Slot and Microstrip Guiding Structures Using Magnetoplasmons for Nonreciprocal Millimeter-Wave Propagation

CLIFFORD M. KROWNE, SENIOR MEMBER, IEEE, AYMAN A. MOSTAFA, STUDENT MEMBER, IEEE, AND KAWTHAR A. ZAKI, SENIOR MEMBER, IEEE

Abstract — **A full-wave spectral-domain approach for general anisotropy is used to determine the nonreciprocal phase and attenuation properties of slot and microstrip line structures. Dominant mode dispersive behavior is controlled by the semiconductor substrate characteristics, geometric dimensions, and magnetic field bias magnitude and angle in the Voigt configuration. Numerical results are presented to establish the nonreciprocal properties up to 85 GHz.**

I. Introduction

HERE WE PROVIDE a study of nonreciprocity in slot and microstrip planar structures compatible with millimeter-wave integrated circuit technology. The approach uses a semiconductor to provide a carrier plasma which is then subjected to a static magnetic field $\vec{B}_0$. The resulting nondiagonalized form of the semiconductor macroscopic tensor $\hat{\epsilon}$ and the field displacement effect [1] lead to different propagation constants γ in the forward γ^+ and reverse γ^- directions. These unequal γ's may contain unequal phase propagation constants (β^+ and β^-) and attenuation constants (α^+ and α^-). Therefore, both β's and α's are studied to find their absolute values and differences $\Delta\alpha = \alpha^+ - \alpha^-$ and $\Delta\beta = \beta^+ - \beta^-$ as functions of ϕ, B_0, T, and geometric dimensions. Here ϕ and T are, respectively, the angle of the field in relation to the planar interfaces (inclination angle) and the ambient lattice temperature.

In contrast to the large number of studies done in the past using the Faraday configuration, which requires polarizers to obtain isolator action based upon $\Delta\alpha = 0$, here the focus is entirely on the use of the Voigt configuration, where $\vec{B}_0$ is perpendicular to the direction of propagation. Several recent theoretical investigations [2]–[5] employing the Voigt configuration have examined open, infinite-in-extent layered structures propagating surface waves guided by the dielectric–semiconductor interfaces. The frequency range was from several hundred GHz up to a maximum of between 700 and 1100 GHz. The semiconductor material utilized was GaAs at 77 K and 10^{15} cm^{-3} n-type doping, implying a particular scattering momentum relaxation time τ_p. Many branches were found for the structures with B_0 in one orientation, namely parallel to the planar layers ($\phi = 0°$); B_0 had been set to ≈ 3800 G. An attempt to direct attention toward the millimeter-wave frequency regime was made more recently by another study which treated a semiconductor-loaded waveguide structure [6]. This work considered Si and GaAs semiconductors, B_0 fields up to 10 kG, and several doping densities. Again the Voigt configuration was considered (with $\phi = 0°$). The theoretical analysis used a few waveguide modes. Both theory and experiment had been done at 92 GHz.

Manuscript received April 4, 1988; revised July 13, 1988. This work was supported in part by the NRL under Contract N00014-86K-2013.

C. M. Krowne is with the Electronics Science and Technology Division, Naval Research Laboratory, Washington, DC 20375-5000.

A. A. Mostafa and K. A. Zaki are with the Department of Electrical Engineering, University of Maryland, College Park, MD 20742.

IEEE Log Number 8824167.

II. Magnetoplasma Permittivity Tensor

In this paper the issue of nonreciprocal guided wave propagation in slot and microstrip structures for MMIC's is addressed. The structures are covered and have electric side walls normal to the layers. All conductors are assumed perfect. A full-wave analysis is used which can handle very general linear macroscopic tensors for the layers [7], [8]. Here the anisotropy is restricted to the semiconductor ($\hat{\epsilon}$). A Drude model [9] is employed to describe the individual electron motion in the semiconductor by

$$m^* \frac{d\boldsymbol{v}}{dt} = q(\boldsymbol{E} + \boldsymbol{v} \times \boldsymbol{B}) - \frac{m^* \boldsymbol{v}}{\tau_p} \tag{1}$$

where q, m^*, and τ_p are, respectively, the electron charge, the effective mass, and the momentum relaxation time. Electron velocity $\boldsymbol{v}$ and fields $\boldsymbol{E}$ and $\boldsymbol{B}$ include dc and RF components. Electron particle current density is

$$\boldsymbol{J} = qn\boldsymbol{v} \tag{2}$$

with n being the electron density and q the electronic charge.

Particle current density $\boldsymbol{J}$ and n also contain dc and RF components. Decomposition of the variables into dc and RF parts is expressed as [10]

$$\boldsymbol{E} = \boldsymbol{E}_0 + \boldsymbol{E}_{\text{RF}} e^{j\omega t - \gamma z} \tag{3a}$$

$$\boldsymbol{B} = \boldsymbol{B}_0 + \boldsymbol{B}_{\text{RF}} e^{j\omega t - \gamma z} \tag{3b}$$

$$\boldsymbol{J} = \boldsymbol{J}_0 + \boldsymbol{J}_{\text{RF}} e^{j\omega t - \gamma z} \tag{3c}$$

$$\boldsymbol{v} = \boldsymbol{v}_0 + \boldsymbol{v}_{\text{RF}} e^{j\omega t - \gamma z} \tag{3d}$$

$$n = n_0 + n_{\text{RF}} e^{j\omega t - \gamma z} \tag{3e}$$

where ω and γ are, respectively, the electromagnetic radian frequency and the propagation constant in the z direction. For the case under study, with no electric field, current, or voltage dc biases, $\boldsymbol{E}_0 = 0$, $\boldsymbol{J}_0 = 0$, and $\boldsymbol{v}_0 = 0$. However, there is an applied dc magnetic field $\boldsymbol{B}_0$ given by

$$\boldsymbol{B}_0 = B_0[\cos(\phi), \sin(\phi), 0]^T = B_0\hat{\boldsymbol{B}}_0. \quad (4)$$

Inserting (3) into (1) and (2), extracting out the zeroth- and first-order perturbations, and dropping all higher order nonlinear terms yields

$$0 = q\boldsymbol{E}_0 + q\boldsymbol{v}_0 \times \boldsymbol{B}_0 - \frac{m^*\boldsymbol{v}_0}{\tau_p} \quad (5a)$$

$$\boldsymbol{J}_0 = qn_0\boldsymbol{v}_0 \quad (5b)$$

and

$$m^*\left(j\omega + \frac{1}{\tau_p}\right)\boldsymbol{v}_{\mathrm{RF}} = q\boldsymbol{E}_{\mathrm{RF}} + q\boldsymbol{v}_{\mathrm{RF}} \times \boldsymbol{B}_0 \quad (6a)$$

$$\boldsymbol{J}_{\mathrm{RF}} = q(n_0\boldsymbol{v}_{\mathrm{RF}} + n_{\mathrm{RF}}\boldsymbol{v}_0) = qn_0\boldsymbol{v}_{\mathrm{RF}}. \quad (6b)$$

Equations (5) are trivially satisfied by the chosen dc bias conditions, while the RF current $\boldsymbol{J}_{\mathrm{RF}}$ in (6b) is simply related by a dc electron proportionality constant to $\boldsymbol{v}_{\mathrm{RF}}$. Eliminating $\boldsymbol{v}_{\mathrm{RF}}$ from (6a) using (6b), and defining the plasma ω_p and cyclotron ω_c radian frequencies as

$$\omega_p^2 = \frac{q^2 n_0}{m^*\epsilon} \quad (7a)$$

$$\omega_c = \frac{qB_0}{m^*} \quad (7b)$$

where ϵ is the static semiconductor permittivity, allows a single governing field equation to be written:

$$\left(j\omega + \frac{1}{\tau_p}\right)\boldsymbol{J}_{\mathrm{RF}} = \epsilon\omega_p^2\boldsymbol{E}_{\mathrm{RF}} + \omega_c\boldsymbol{J}_{\mathrm{RF}} \times \hat{\boldsymbol{B}}_0. \quad (8)$$

The dc magnetic field unit vector $\hat{\boldsymbol{B}}_0$ is defined by (4). Governing equation (8) is recast as

$$\boldsymbol{E}_{\mathrm{RF}} = \hat{\rho}\boldsymbol{J}_{\mathrm{RF}} \quad (9)$$

so that the macroscopic resistivity tensor $\hat{\rho}$ is determined as

$$\hat{\rho} = \begin{bmatrix} j\omega + \tau_p^{-1} & 0 & \omega_c \sin\phi \\ 0 & j\omega + \tau_p^{-1} & -\omega_c\cos\phi \\ -\omega_c\sin\phi & \omega_c\cos\phi & j\omega + \tau_p^{-1} \end{bmatrix} \frac{1}{\epsilon\omega_p^2}. \quad (10)$$

The requirement of a sourceless field problem and a single 6×6 constitutive tensor $\hat{M}$ relating $\boldsymbol{E}_{\mathrm{RF}}$, $\boldsymbol{D}_{\mathrm{RF}}$, $\boldsymbol{H}_{\mathrm{RF}}$, and $\boldsymbol{B}_{\mathrm{RF}}$ [7] leads to permeability $\hat{\mu} = I\mu_0$ (μ_0 = vacuum value), optical activities $\hat{\rho}_o = \hat{\rho}_o' = 0$, and permittivity determined as follows. Maxwell's curl $\boldsymbol{H}$ equation is

$$\nabla \times \boldsymbol{H} = \frac{\partial \boldsymbol{D}}{\partial t} + \boldsymbol{J} \quad (11)$$

where $\boldsymbol{D}$ is the electric displacement vector field. Here

$$\boldsymbol{D} = \epsilon\boldsymbol{E}, \quad (12a)$$

$$\boldsymbol{H} = \mu_0^{-1}\boldsymbol{B}. \quad (12b)$$

Placing (9) and (12) into (11), utilizing (3), and retaining the first-order perturbation gives

$$\nabla \times \boldsymbol{H}_{\mathrm{RF}} = (j\omega\epsilon + \hat{\rho}^{-1})\boldsymbol{E}_{\mathrm{RF}} \quad (13)$$

leading to the permittivity (in what comes below, the RF subscripts will be understood and so dropped in the equations):

$$\hat{\epsilon} = \epsilon I + \frac{\hat{\sigma}}{j\omega}, \qquad \hat{\sigma} = \hat{\rho}^{-1}. \quad (14)$$

For GaAs, Γ electron valley effective masses are appropriate to use so that

$$\omega_c = 2.63 \times 10^{11} B_0 (10^3 \text{ kG}) \quad (15a)$$

$$\omega_p = 1.93 \times 10^{13}\sqrt{n(10^{17}/\text{cc})}\,. \quad (15b)$$

Attenuation arises from the finite value of the momentum relaxation time τ_p in (10). The off-diagonal $\hat{\rho}$ elements cause $\Delta\alpha$ and $\Delta\beta$ to be nonzero for finite B_0. Relaxation time τ_p can be estimated by a single formula:

$$\tau_p = 3.8048T^{-0.7361}[20.133 - \log(N_I)](\text{ps}) \quad (15c)$$

which takes into account ionized impurity scattering (N_I = ionized density) and phonon scattering. Equation (15c) is based upon experimental and theoretical results for GaAs [11], [12] at lattice temperatures between 77 and 300 K. Numerical calculations done in this paper under different physical parameter conditions are roughly consistent with (15c) for τ_p if the semiconductor is envisioned as GaAs. For full ionization, $n_0 = N_D$ (donor doping) $= N_I$.

III. Slot Admittance Anisotropic Dyadic

An admittance-type anisotropic dyadic Green's function, in the spectral domain, is used to relate surface current $\tilde{J}$ to tangential electric field $\tilde{E}$ at the conductor–slot interface. The one-dimensional finite Fourier transform of an arbitrary two-dimensional spatial function $f(x, y)$ is

$$\tilde{f}(\alpha_n, y) = \int_{-b/2}^{b/2} f(x, y)e^{-j\alpha_n x}\,dx \quad (16)$$

where y = interface and $\alpha_n = (2n-1)\pi/b$ or $2n\pi/b$ for even or odd modes, respectively, with n = any integer. Thus

$$\tilde{J}_x(n) = \tilde{G}_{11}'(\gamma, n)\tilde{E}_x(n) + \tilde{G}_{12}'(\gamma, n)\tilde{E}_z(n) \quad (17a)$$

$$\tilde{J}_z(n) = \tilde{G}_{21}'(\gamma, n)\tilde{E}_x(n) + \tilde{G}_{22}'(\gamma, n)\tilde{E}_z(n). \quad (17b)$$

Dyadic $\tilde{G}' = \tilde{G}^{-1}$, $\tilde{G}$ being the impedance anisotropic dyadic [8]. Slot electric field components are expanded in terms of complete trigonometric basis function sets satisfying the edge condition. For single slot even and odd modes with respect to E_z, we use, respectively, the basis functions

$$E_{xm}(x) = \eta_{em}(x) = R^{-1}\sin\left[(2m-1)\frac{\pi x}{w}\right] \quad (18a)$$

$$E_{zm}(x) = \xi_{em}(x) = R^{-1}\cos\left[(2m-1)\frac{\pi x}{w}\right] \quad (18b)$$

and

$$E_{xm}(x) = \eta_{om}(x) = R^{-1}\cos\left[(m-1)\frac{2\pi x}{w}\right] \quad (19a)$$

$$E_{zm}(x) = \xi_{om}(x) = R^{-1}\sin\left[\frac{2\pi x m}{w}\right] \quad (19b)$$

for $|x| \leqslant w/2$ with $m = 1, 2, \cdots$, and $R = [1-(2x/w)^2]^{1/2}$, and the right-hand-sides of (18) and (19) are zero otherwise.

The finite Fourier transforms of (18) and (19) are

$$\tilde{E}_{xm}(n) = \tilde{\eta}_{em}(n) = -\frac{j\pi w}{4} \cdot \left[J_0\left(\alpha_n\frac{w}{2} + (2m-1)\frac{\pi}{2}\right) - J_0\left(\alpha_n\frac{w}{2} - (2m-1)\frac{\pi}{2}\right)\right] \quad (20a)$$

$$\tilde{E}_{zm}(n) = \tilde{\xi}_{em}(n) = \frac{\pi w}{4} \cdot \left[J_0\left(\alpha_n\frac{w}{2} + (2m-1)\frac{\pi}{2}\right) + J_0\left(\alpha_n\frac{w}{2} - (2m-1)\frac{\pi}{2}\right)\right] \quad (20b)$$

for the even mode and

$$\tilde{E}_{xm}(n) = \tilde{\eta}_{om}(n) = \frac{\pi w}{4} \cdot \left[J_0\left(\alpha_n\frac{w}{2} + (m-1)\pi\right) + J_0\left(\alpha_n\frac{w}{2} - (m-1)\pi\right)\right] \quad (21a)$$

$$\tilde{E}_{zm}(n) = \tilde{\xi}_{om}(x) = -\frac{j\pi w}{4} \cdot \left[J_0\left(\alpha_n\frac{w}{2} + m\pi\right) - J_0\left(\alpha_n\frac{w}{2} - m\pi\right)\right] \quad (21b)$$

for the odd mode. J_0 is the Bessel function of the first kind and zeroth order. Total slot spectral fields are then

$$\tilde{E}_x(n) = \sum_{m=1}^{n_x} p_m \tilde{E}_{xm}(n) \quad (22a)$$

$$\tilde{E}_z(n) = \sum_{m=1}^{n_z} q_m \tilde{E}_{zm}(n). \quad (22b)$$

Inserting (22) into (17), applying Parseval's theorem, and using a Galerkin approach, a determinantal equation for the propagation constant can be written based on the fact that the slot electric field expansion coefficients are not a trivial null set. Numerical results below are found by setting maximum x and z field expansion indices n_x and n_z to 1 with maximum $n \approx 10^2$ (larger n_x and n_z values have been tested to ensure solution convergence). Construction of coupled slot electric fields is covered in Appendix I. Derivation of the coupled slot anisotropic determinantal equation is given in Appendix II.

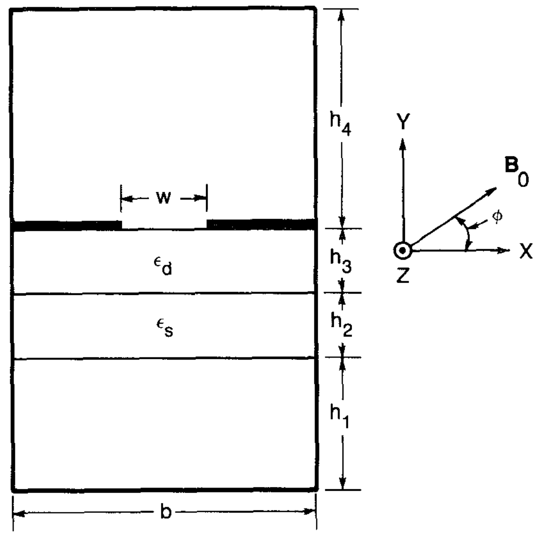

Fig. 1. Cross section of a single suspended slot line structure. Magnetic field bias B_0 is at inclination angle ϕ to the planar surfaces.

IV. Numerical Results

Fig. 1 shows a sketch of a suspended single slot line structure. Electromagnetic propagation is either in the z direction, out of the paper ("+" or forward direction), or into the paper ("−" or reverse direction). The suspended single slot line rests on two substrates, a dielectric with relative permittivity $\epsilon_d = 12.5$ and the semiconductor with $\epsilon_s = \epsilon_d$. Regions of thickness h_1 and h_4 are air (relative permittivity $\epsilon_{r1} = \epsilon_{r4} = 1$, relative permeability $\mu_r = 1$). Slot width $w = 1.0$ mm, and the other geometric dimensions are $b = 2.35$ mm, $h_1 = h_4 = 2.1$ mm, and $h_2 = 0.25$ mm. Thickness h_3 is varied. Numerical results are first presented for $\phi = 0°$, with $\omega_c = 3.14 \times 10^{12}$ rad/s ($B_0 = 12$ kG), $\omega_p = 6.28 \times 10^{12}$ rad/s ($n_0 = 10^{16}$/cc), and $\tau_p = 10^{-13}$ s (room-temperature operation). Only the dominant mode is calculated and discussed here. This mode is odd with respect to E_z and even with respect to E_x. In the $B_0 \to 0$ limit, the regular dominant slot line mode is obtained.

Fig. 2 shows α(dB/mm) (with $\alpha = \alpha^+$ or α^-) versus frequency f (GHz) between 45 and 85 GHz for $h_3 = 0.25$ mm. At the α peaks, $\Delta\alpha/\alpha \approx 15$ percent. The normalized phase propagation constant $\bar{\beta} = \beta/\beta_0$ with $\beta = \beta^+$ or β^-, β_0 = free-space value, is shown in Fig. 3(a) and (b) for, respectively, $h_3 = 0.25$ mm and $h_3 = 0$ mm. It is evident that $\Delta\bar{\beta}$ increases with decreasing h_3 by comparing Fig. 3(a) and (b) (and this is particularly apparent in Fig. 5 to follow). Such behavior is physically understandable since h_3 reduction places the magnetoplasma layer in closer proximity to the slot. Here $\Delta\bar{\beta}/\bar{\beta} \approx 1.3$ percent across the 45 through 80 GHz frequency range displayed ($h_3 = 0$). Figs. 4 and 5 plot, respectively, $\Delta\alpha$ and $\Delta\beta$ versus f between 45 and 75 GHz for h_3 parameterized, $h_3 = 0$, 0.01, 0.1, and 0.25 mm. Attenuation difference $\Delta\alpha$ increases with f, but is insensitive to h_3 variation (Fig. 4).

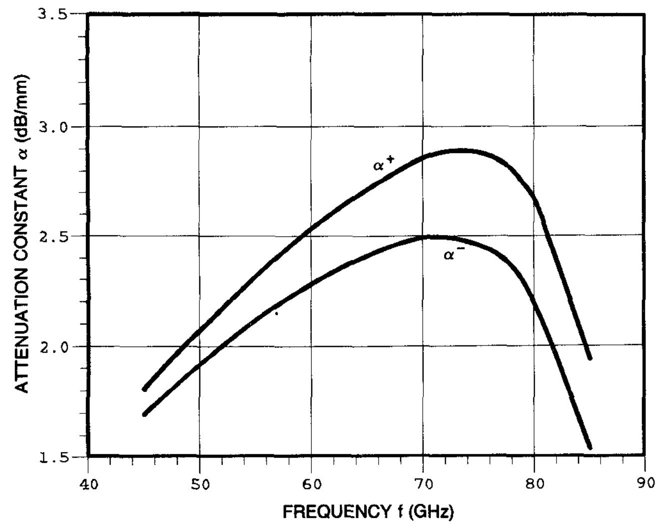

Fig. 2. Dispersion behavior of α^+ and α^- for the odd mode of single suspended slot line. $B_0=12$ kG, $\phi=0°$, $n_0=10^{16}$/cc, $\tau_p=0.1$ ps, $w=1.0$ mm, $h_1=h_4=2.1$ mm, $h_2=h_3=0.25$ mm, $\epsilon_s=\epsilon_d=12.5$.

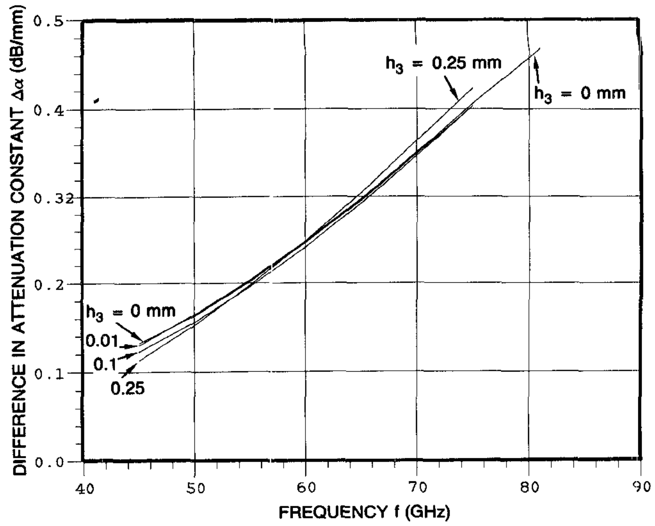

Fig. 4. Dispersion behavior of $\Delta\alpha$, with parameterized $h_3=0$, 0.01, 0.1, and 0.25 mm.

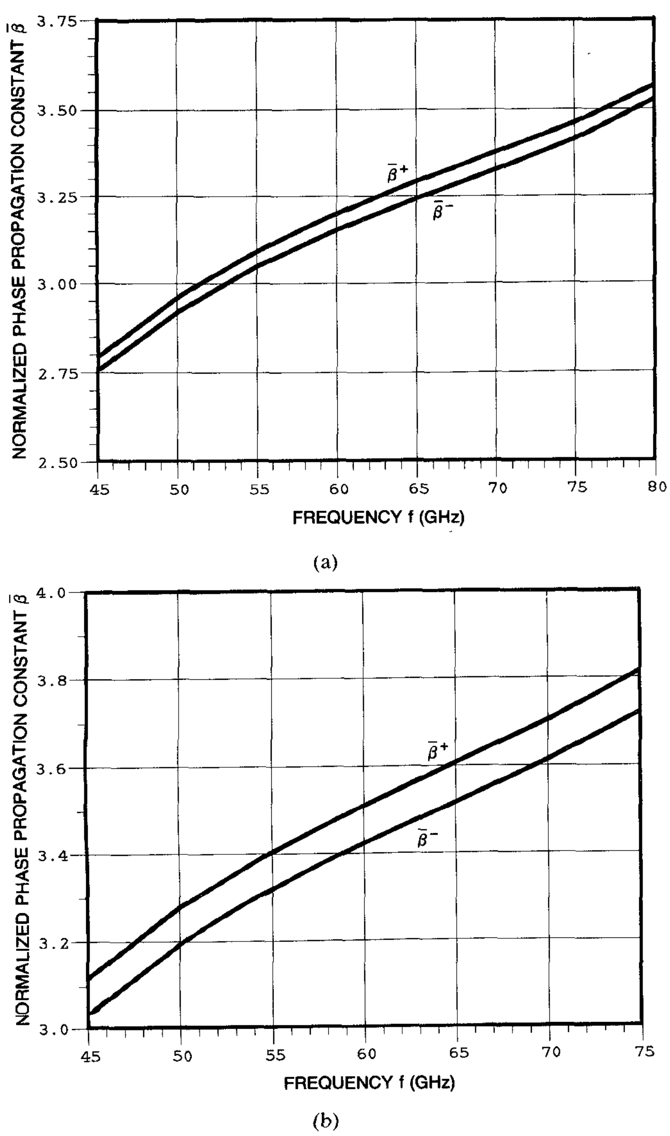

Fig. 3. (a) Dispersion behavior of $\bar{\beta}^+$ and $\bar{\beta}^-$. Parameters are the same as in Fig. 2. (b) Dispersion behavior of $\bar{\beta}^+$ and $\bar{\beta}^-$. Parameters are as in Fig. 3(a) except $h_3=0$ mm.

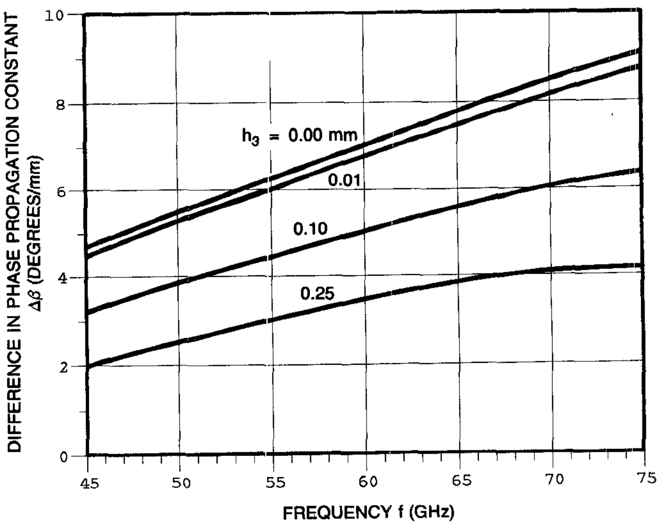

Fig. 5. Dispersion behavior of $\Delta\beta$, with h_3 parameterized.

For $f=75$ GHz, Figs. 6 and 7 show α and $\bar{\beta}$ under varying ϕ. Notice the monotonic decrease of $\Delta\alpha$ and $\Delta\bar{\beta}$ with increasing ϕ, and $\alpha^+>\alpha^-$ and $\bar{\beta}^+>\bar{\beta}^-$. For the choice of parameters selected, $\Delta\alpha$, $\Delta\bar{\beta}$, α^-, $\bar{\beta}^+$ and $\bar{\beta}^-$ are all roughly constant up to 15° inclination angle. The attenuation constant α^+ hardly varies (compared to α^-) up to $\phi=60°$. As $\phi\to 90°$, both $\Delta\alpha$ and $\Delta\beta$ approach zero. An explanation for such a limiting characteristic is the creation of cyclotron electron orbits which are perpendicular to the B_0 direction and parallel to the planar interfaces. With $\phi=0°$, Fig. 8(a) and (b) provides $\bar{\alpha}$ and $\bar{\beta}$, respectively, for varying B_0 up to 16 kG.

Four other planar structures in Fig. 9 are now examined for their dominant mode behavior with $\phi=0°$, two slot and two microstrip (see [8] for the forms of the single and coupled microstrips surface currents used in the anisotropic determinantal equation for γ solution). First the even

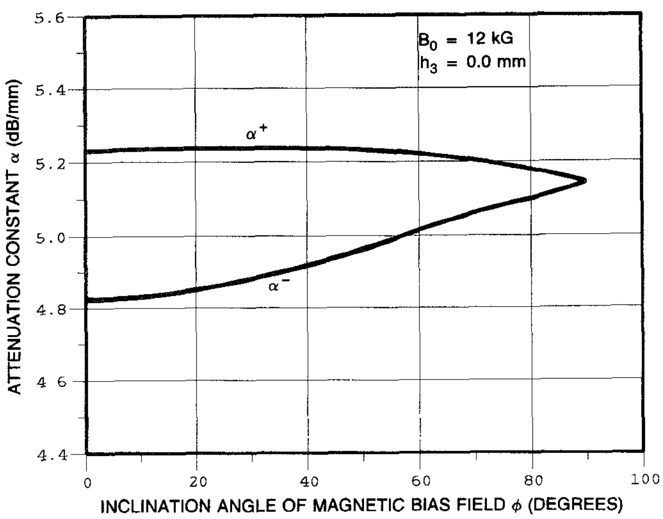

Fig. 6. Variation of α^+ and α^- with inclination angle ϕ.

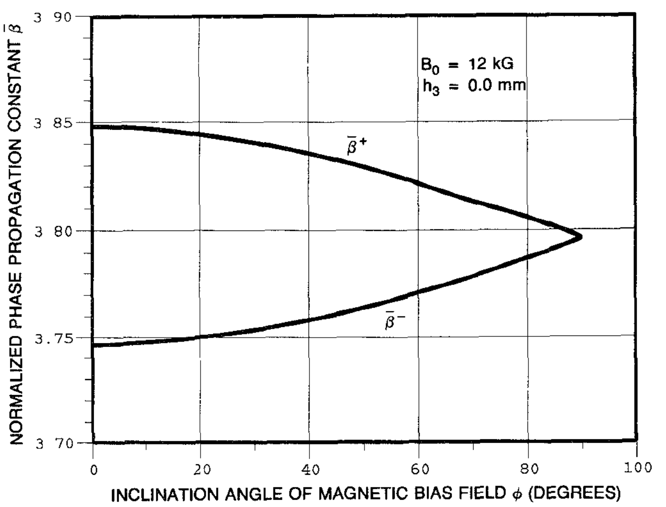

Fig. 7. Variation of β^+ and β^- with inclination angle ϕ

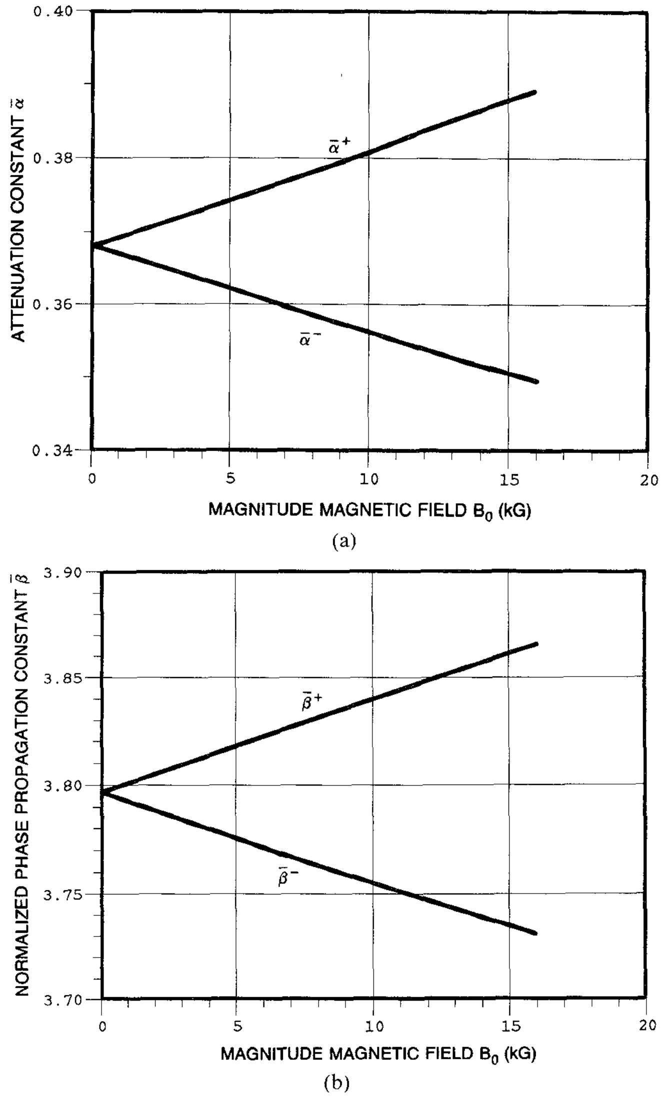

Fig. 8. (a) Variation of $\bar{\alpha}^+$ and $\bar{\alpha}^-$ with magnetic field B_0. $h_3 = 0.0$ mm. (b) Variation of $\bar{\beta}^+$ and $\bar{\beta}^-$ with magnetic field B_0. $h_3 = 0\ 0$ mm.

mode of the suspended coupled slot structure in Fig. 9(a) is studied for the same geometrical and physical parameters as in Fig. 8 except $w = w_1 = 0.2$ mm ($h_3 = 0$ mm and $f = 75$ GHz). Fig. 10(a) and (b) shows the α and $\bar{\beta}$ variation versus B_0: $\Delta\alpha/\alpha \approx 14.2$ percent and $\Delta\bar{\beta}/\bar{\beta} \approx 1.6$ percent at $B_0 = 10$ kG. Secondly the odd mode of the sandwiched suspended single slot structure in Fig. 9(b) was studied under a varying B_0 field for the same parameters as in Fig. 10 except $h_2 = h_3 = 0.25$ mm and $w = 1.0$ mm. One finds that $\alpha(0\text{ kG}) = 3.196$ dB/mm, $\bar{\beta}$ (0 kG) = 3.173, $\alpha^-(12\text{ kG}) = 2.965$ dB/mm, $\bar{\beta}^-(12\text{ kG}) = 3.155$, and $\Delta\alpha/\alpha = 15.2$ percent and $\Delta\bar{\beta}/\bar{\beta} = 1.1$ percent at 12 kG. Intermediate $\gamma(B_0)$ values are easily found due to the linearity of the curves and the ordering property $\alpha^+ > \alpha^-, \bar{\beta}^+ > \bar{\beta}^-$. The ordering property occurs for most of our results and associates greater slowing with higher attenuation. Comparison to the normalized attenuation constant $\bar{\alpha} = \alpha/\beta_0$ in Fig. 8(a) indicates about a 40 percent reduction in α, suggesting that the addition of a dielectric cover of this thickness removes much of the field intensity from the semiconductor. On the other hand, thinning h_3 to $h_3 = 0.10$ mm increases α by about 25 percent, an effect which may be attributed to pulling the fields into closer proximity to the slot region. One has α (0 kG) = 6.77 dB/mm, $\alpha^-(14\text{ kG}) = 6.502$ dB/mm, and $\Delta\alpha/\alpha = 8.2$ percent. Fig. 11(a) and (b) shows the behavior of α and $\bar{\beta}$ as h_2 is varied from about 0.07 mm to 1.2 mm at $B_0 = 12$ kG with $h_3 = 0.10$ mm and $w = 1.0$ mm (Fig. 9(b) structure; other parameters the same as in Fig. 10). Here $\alpha^{+,-}$ first rises (as expected since $\alpha \equiv 0$ at $h_2 = 0$), then monotonically decreases—similar behavior is observed for $\bar{\beta}$. The precipitous, then gradual decrease of $\gamma^{+,-}$ with h_2 is related to the reduction of fields located in the slot vicinity. Thirdly the even mode of the suspended single microstrip structure in Fig. 9(c) is analyzed under a varying B_0 field for the same parameters as in Fig. 10 except $h_3 = 0$ mm and $w_1 = 0.2$ mm. It is found that γ depends linearly on B_0 and that $\alpha(0\text{ kG}) = 4.021$ dB/mm, $\alpha^-(10\text{ kG}) = 3.832$ dB/mm, and $\Delta\alpha/\alpha = 9.8$ percent at 10 kG. Shrinking w_1 to 0.0125 mm causes α reduction ($\alpha(0\text{ kG}) =$

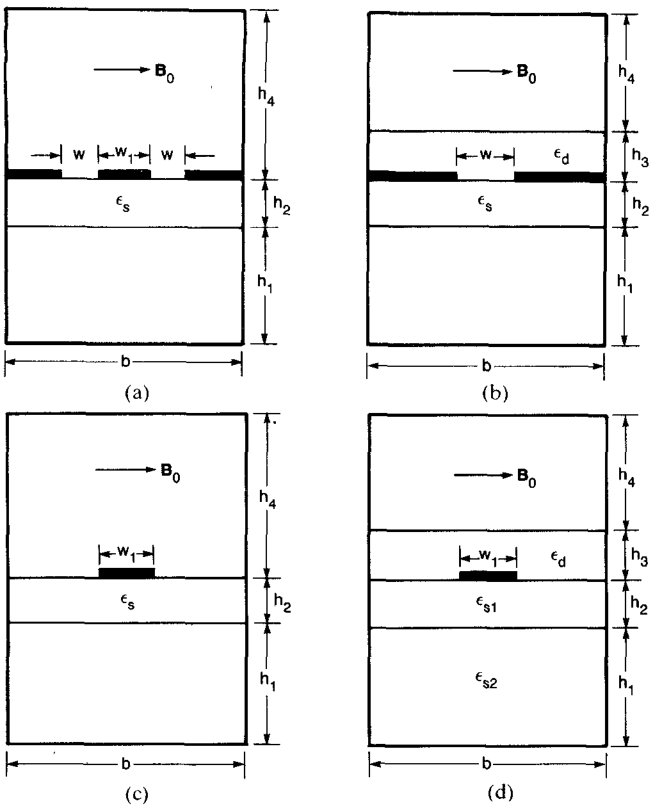

Fig. 9. Cross sections of planar structures possessing a semiconductor(s) under dc magnetic field bias B_0 and inclination angle $\phi = 0°$. The gyroelectric effect is studied in (a) suspended coupled slot line, (b) sandwiched suspended single slot line, (c) suspended single microstrip, and (d) covered single microstrip.

2.835 dB/mm, $\alpha^-(12\text{ kG}) = 2.631$ dB/mm) but $\Delta\alpha/\alpha =$ 15.8 percent at 12 kG.

The last structure examined is the dielectric-covered single microstrip over a doped semiconductor layer of thickness $h_2 = 0.25$ mm and an undoped substrate of thickness $h_1 = 2.1$ mm ($= h_4$). It is shown in Fig. 9(d). Here the cover has $h_3 = 0.1$ mm, $w_1 = 0.2$ mm, and $\epsilon_d = \epsilon_{s1} = \epsilon_{s2} = 12.5$. Fig. 12(a) and (b) gives α and $\bar{\beta}$ versus B_0 up to nearly 35 kG at $f = 50$ GHz with $\omega_p = 6.28 \times 10^{11}$ rad/s ($n_0 = 10^{14}$/cc). The even mode results are parameterized in terms of $\tau_p = (1,5,10) \times 10^{-13}$s. At low B_0, α increases as τ_p increases, an effect not seen beyond 5 kG. As $\tau_p \to \infty$, $\alpha \to 0$ (not shown), as expected for no carrier scattering. The quantity $\Delta\alpha$ first increases then decreases with rising B_0. Maximum $\Delta\alpha \approx 1.4$ dB/mm and occurs for $3 \lesssim B_0 \lesssim 7$ kG with $\tau_p = 10^{-12}$s. This corresponds to a $\Delta\alpha/\alpha \approx 47$ percent at 5 kG. One notices that these curves are extremely nonlinear for $B_0 < 20$ kG and $\tau_p \neq 10^{-13}$s. Highly nonlinear behavior is mimicked in the $\bar{\beta}$ versus B_0 curves for $B_0 < 20$ kG and $\tau_p \neq 10^{-13}$s (Fig. 12(b)). Beyond 20 kG, $\Delta\bar{\beta}$ is approximately constant and $\bar{\beta}$ behaves linearly. Attenuation dependence of α on τ_p at $B_0 = 20$ kG is presented in Figs. 13(a) and (b) for different $n_0 = 10^{12}$, 10^{13}, and 10^{14}/cc. As $\tau_p \to 10^{-14}$s, both α and $\Delta\alpha$ decrease. Also as expected, α and $\Delta\alpha$ tend to decrease as τ_p gets large (beyond $\tau_p = 10^{-11}$s for $n_0 = 10^{14}$/cc). However, $\Delta\alpha/\alpha \approx 130$ percent near $\tau_p = 6.2 \times 10^{-12}$s. When n_0 increases, the absolute α maxima move to the left (or smaller τ_p). Fig. 14 presents the corresponding $\bar{\beta}$ versus τ_p dependence. $\Delta\bar{\beta}$ increases with increasing n_0. For $n_0 = 10^{14}$/cc, $\Delta\bar{\beta} \approx$ constant up to $\tau_p = 2.5 \times 10^{-12}$s, beyond which it monotonically increases to $\Delta\bar{\beta}/\bar{\beta} \approx 11$ percent. Fig. 15(a) and (b) provides α and $\bar{\beta}$ against h_2 for $B_0 = 10$ kG, $\tau_p = 10^{-13}$s, and $w_1 = 0.2$ mm with parameterized h_3.

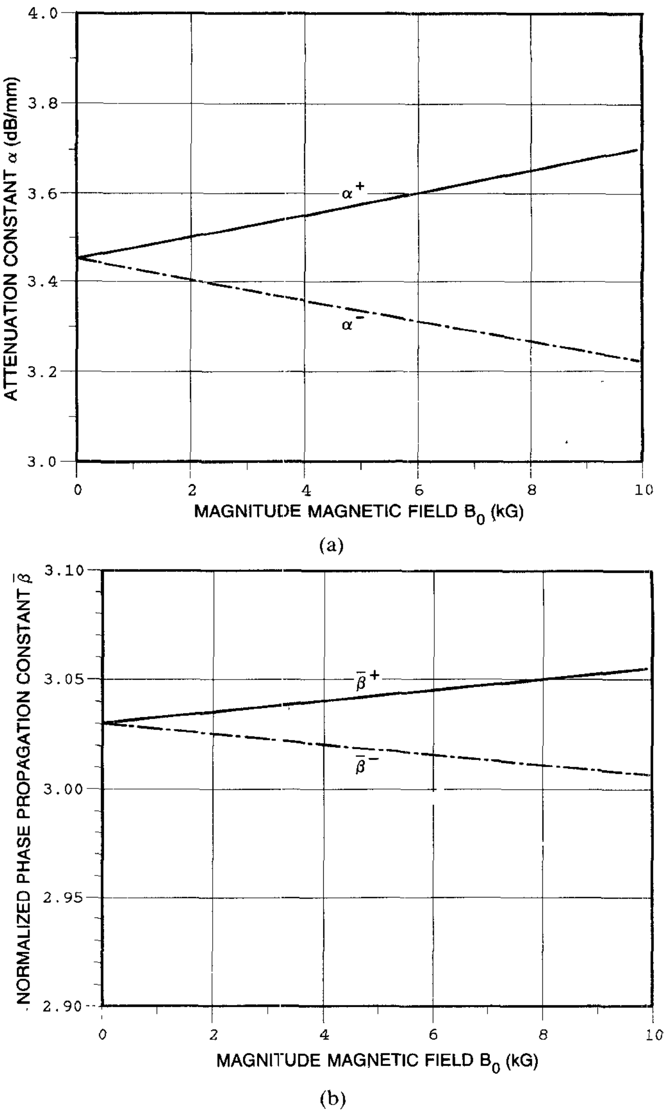

Fig. 10. (a) Variation of α^+ and α^- with magnetic field B_0 for the even mode of the suspended coupled slot structure (Fig. 9(a)). Same parameters as used in Fig. 2 except $h_3 = 0$ mm, $w = w_1 = 0.2$ mm, and $f = 75$ GHz. (b) Variation of $\bar{\beta}^+$ and $\bar{\beta}^-$ with magnetic field B_0 for the Fig. 10(a) case.

V. Conclusion

A full-wave matrix spectral-domain approach for complex anisotropy is used to find the propagation constants in the forward and reverse directions for suspended single slot line layered structures. A dc bias magnetic field B_0 is employed to generate permittivity anisotropy in the semiconductor layer. The B_0 field is normal to the propagation direction, and its inclination angle ϕ to the interface is varied. Numerical results between 45 and 85 GHz for a GaAs semiconductor layer are obtained. Differences between forward and reverse attenuation constants (dB/λ_0)

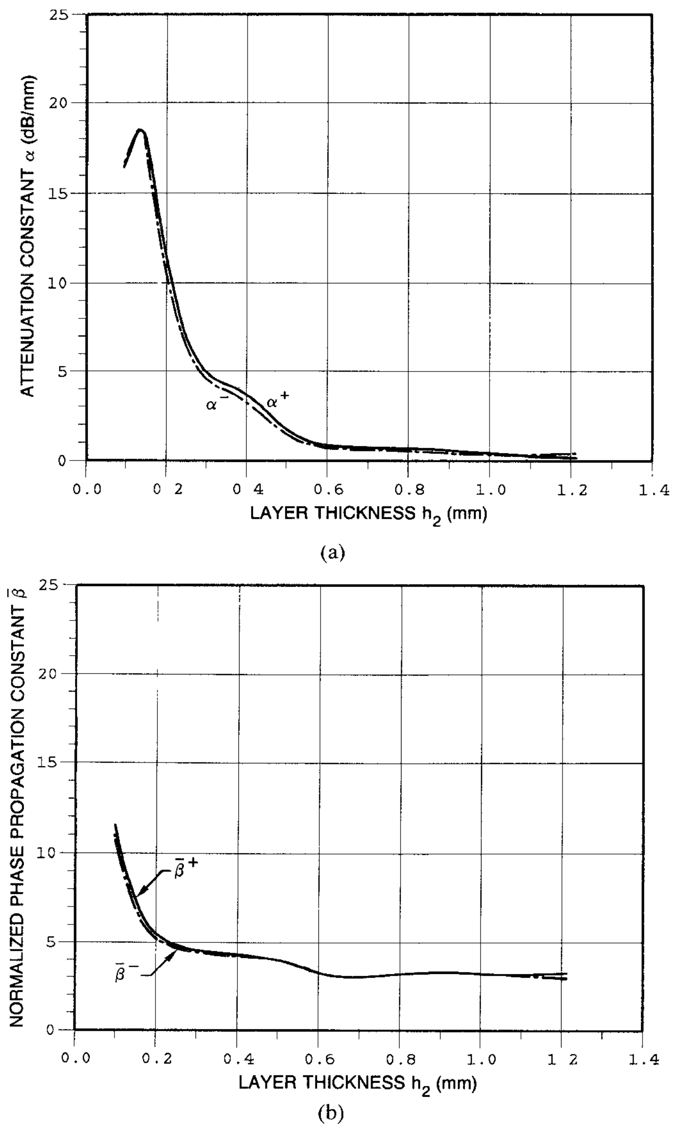

Fig 11. (a) Variation of α^+ and α^- against h_2 for the even mode of the sandwiched suspended single slot structure (Fig. 9(b)). Same parameters as in Fig. 10 except $h_3 = 0.10$ mm, $w = 1.0$ mm, and $B_0 = 12$ kG. (b) Variation of $\bar{\beta}^+$ and $\bar{\beta}^-$ against h_2 for the Fig. 11(a) case.

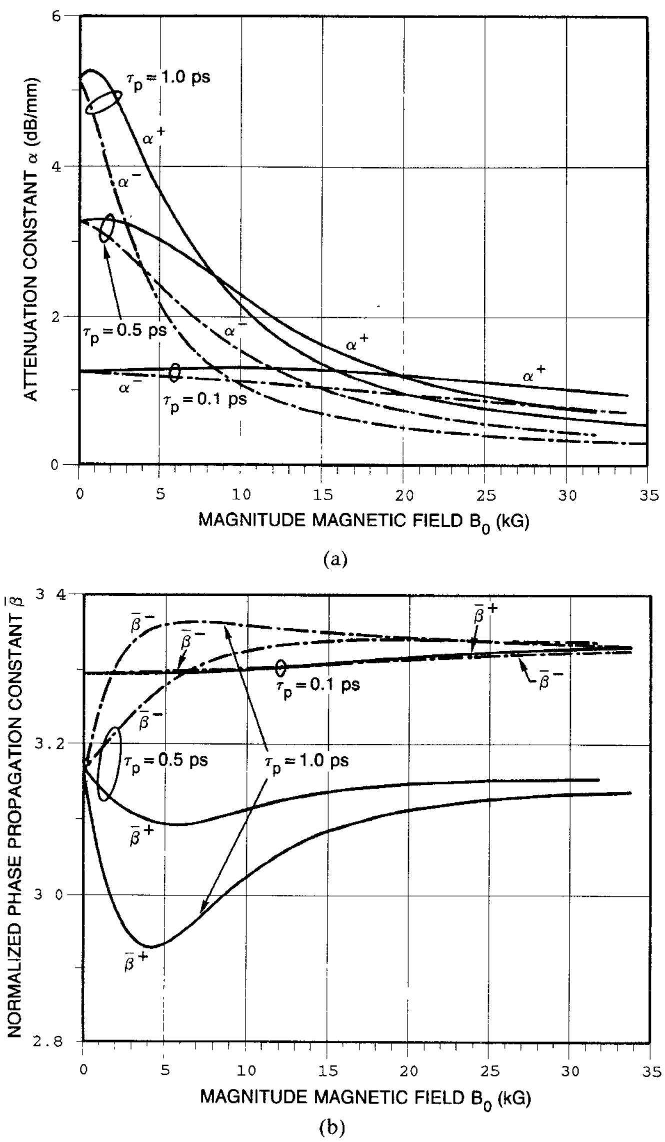

Fig. 12. (a) Variation of α^+ and α^- with magnetic field B_0 for the even mode of the covered single microstrip structure (Fig. 9(d)). Parameters same as in Fig. 11 except that here $h_2 = 0.25$ mm, $h_3 = 0.10$ mm, $\epsilon_d = \epsilon_{s1} = \epsilon_{s2} = 12.5$, $n_0 = 10^{14}$/cc, and $f = 50$ GHz. Results are parameterized in τ_p. (b) Variation of $\bar{\beta}^+$ and $\bar{\beta}^-$ with magnetic field B_0 for the Fig. 12(a) case.

and phase constants (degrees/λ_0) show increases with increasing frequency. These differences apear to be largest, though, for small $\phi \lesssim 20°$.

Numerical results are also found for other slot line structures (sandwich suspended single slot and suspended coupled slot) and single microstrip structures (covered microstrip and suspended microstrip) for $\phi = 0°$. Physical parameters of the doped semiconductor such as n_0 and τ_p as well as B_0 and geometric parameters are varied to characterize nonreciprocal effects.

Appendix I

Coupled slot electric field (only within the slots, zero otherwise) are expressed as

$$E_x(x) = \sum_{m=1}^{n_x} \{a_{m1}\eta_{em}(x+s) + b_{m1}\eta_{om}(x+s)\} + \sum_{m=1}^{n_x} \{a_{m2}\eta_{em}(x-s) + b_{m2}\eta_{om}(x-s)\} \quad \text{(A1)}$$

$$E_z(x) = \sum_{m=1}^{n_z} \{c_{m1}\xi_{em}(x+s) + d_{m1}\xi_{om}(x+s)\} + \sum_{m=1}^{n_z} \{c_{m2}\xi_{em}(x-s) + d_{m2}\xi_{om}(x-s)\}. \quad \text{(A2)}$$

Here the first summed term in (A1) and (A2) accounts for the slot located at $x = -s$, $s = (w + w_1)/2$, whereas the second term accounts for the slot located at $x = +s$. Basis functions $\eta_{em}, \eta_{om}, \xi_{em}, \xi_{om}$ are even and odd single slot functions provided in (18) and (19).

For the coupled slot even mode case,

$$E_z(x) = E_z(-x) \quad \text{(A3a)}$$

$$E_x(x) = -E_x(-x). \quad \text{(A3b)}$$

Placing (A2) into (A3a) yields, for the mth term,

$$\begin{aligned}&c_{m1}\xi_{em}(x+s)+d_{m1}\xi_{om}(x+s)+c_{m2}\xi_{em}(x-s)\\&\quad+d_{m2}\xi_{om}(x-s)\\&\quad=c_{m1}\xi_{em}(-x+s)+d_{m1}\xi_{om}(-x+s)\\&\qquad+c_{m2}\xi_{em}(-x-s)+d_{m2}\xi_{om}(-x-s)\\&\quad=c_{m1}\xi_{em}(x-s)-d_{m1}\xi_{om}(x-s)\\&\qquad+c_{m2}\xi_{em}(x+s)-d_{m2}\xi_{om}(x+s)\end{aligned}$$

or

$$\begin{aligned}&(c_{m1}-c_{m2})\xi_{em}(x+s)+(d_{m1}+d_{m2})\xi_{om}(x+s)\\&\quad+(c_{m2}-c_{m1})\xi_{em}(x-s)\\&\quad+(d_{m2}+d_{m1})\xi_{om}(x-s)=0\end{aligned}$$

or, more compactly,

$$\begin{aligned}(c_{m1}-c_{m2})[\xi_{em}(x+s)-\xi_{em}(x-s)]+(d_{m1}+d_{m2})\\\cdot[\xi_{om}(x+s)+\xi_{om}(x-s)]=0.\qquad\text{(A4)}\end{aligned}$$

Equation (A4) will only hold if

$$c_{m1}=c_{m2}\qquad d_{m1}=-d_{m2}.\qquad\text{(A5)}$$

Inserting (A5) into (A2) gives the spatial E_z dependence,

$$\begin{aligned}E_z(x)=\sum_{m=1}^{n_z}\{c_{m1}[\xi_{em}(x+s)+\xi_{em}(x-s)]+d_{m1}\\\cdot[\xi_{om}(x+s)-\xi_{om}(x-s)]\}.\qquad\text{(A6)}\end{aligned}$$

Following a similar procedure for $E_x(x)$ produces

$$a_{m1}=-a_{m2}\qquad b_{m1}=b_{m2}\qquad\text{(A7)}$$

and

$$\begin{aligned}E_x(x)=\sum_{m=1}^{n_x}\{a_{m1}[\eta_{em}(x+s)-\eta_{em}(x-s)]+b_{m1}\\\cdot[\eta_{om}(x+s)+\eta_{om}(x-s)]\}.\qquad\text{(A8)}\end{aligned}$$

By employing the Fourier shifting relationships

$$\tilde{\xi}_{e,om}(x\pm s)=e^{\pm j\alpha_n s}\tilde{\xi}_{e,om}(n)\qquad\text{(A9a)}$$

$$\tilde{\eta}_{e,om}(x\pm s)=e^{\pm j\alpha_n s}\tilde{\eta}_{e,om}(n)\qquad\text{(A9b)}$$

where the arguments of the left-hand side variables are present to identify the spatial variables transformed, the final forms of spectral slot electric fields are stated, using (A6) and (A8), as

$$\tilde{E}_x(n)=\sum_{m=1}^{n_x}\{a'_{m1}\sin(\alpha_n s)\tilde{\eta}_{em}+b'_{m1}\cos(\alpha_n s)\tilde{\eta}_{om}\}\qquad\text{(A10a)}$$

$$\tilde{E}_z(n)=\sum_{m=1}^{n_z}\{c'_{m1}\cos(\alpha_n s)\tilde{\xi}_{em}+d'_{m1}\sin(\alpha_n s)\tilde{\xi}_{om}\}.\qquad\text{(A10b)}$$

Here the primed coefficients are related to the old coefficients as follows:

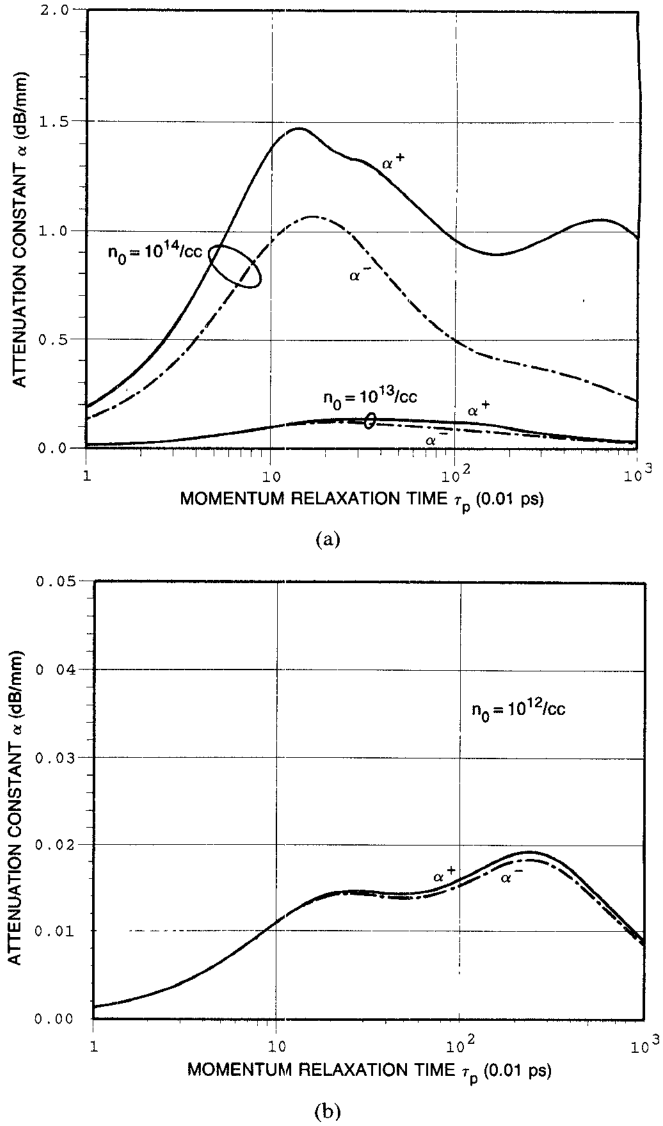

Fig. 13. (a) Variation of α^+ and α^- against τ_p for the Fig. 12(a) case with $B_0 = 20$ kG. Parameterized curves for $n_0 = 10^{13}$ and 10^{14}/cc. (b) Variation of α^+ and α^- against τ_p for the Fig. 13(a) case. $n_0 = 10^{12}$/cc.

$$\begin{aligned}a'_{m1}&=2ja_{m1}\qquad &b'_{m1}&=2b_{m1}\\c'_{m1}&=2c_{m1}\qquad &d'_{m1}&=2jd_{m1}.\end{aligned}\qquad\text{(A11)}$$

For the coupled slot odd mode case,

$$E_z(x)=-E_z(-x)\qquad E_x(x)=E_x(-x).\qquad\text{(A12)}$$

Using the same reasoning process as for the even mode case,

$$\tilde{E}_x(n)=\sum_{m=1}^{n_x}\{a''_{m1}\cos(\alpha_n s)\tilde{\eta}_{em}+b''_{m1}\sin(\alpha_n s)\tilde{\eta}_{om}\}\qquad\text{(A13a)}$$

$$\tilde{E}_z(n)=\sum_{m=1}^{n_z}\{c''_{m1}\sin(\alpha_n s)\tilde{\xi}_{em}+d''_{m1}\cos(\alpha_n s)\tilde{\xi}_{om}\}\qquad\text{(A13b)}$$

where

$$\begin{aligned}a''_{m1}&=2a_{m1}\qquad &b''_{m1}&=2jb_{m1}\\c''_{m1}&=2jc_{m1}\qquad &d''_{m1}&=2d_{m1}.\end{aligned}\qquad\text{(A14)}$$

APPENDIX II

The coupled slot anisotropic determinantal equation is derived as follows. First find a Parseval theorem. At the interface of interest, we drop y in (10) to obtain

$$\Lambda(x) = \frac{1}{b} \sum_{n=-\infty}^{\infty} \tilde{\Lambda}(n) e^{j\alpha_n x} \tag{A15}$$

$$\tilde{\Lambda}(n) = \int_{-b/2}^{b/2} \Lambda(x) e^{-j\alpha_n x}. \tag{A16}$$

Letting $\Lambda = g$ or f,

$$\sum_{n=-\infty}^{\infty} \tilde{f}(n)\tilde{g}(n) = \sum_{n=-\infty}^{\infty} \tilde{g}(n) \int_{-b/2}^{b/2} f(x) e^{-j\alpha_n x}\, dx$$

$$= -\int_{-b/2}^{b/2} f(-x') \left[\sum_{n=-\infty}^{\infty} \tilde{g}(n) e^{j\alpha_n x'} \right] dx'$$

$$= -b \int_{-b/2}^{b/2} f(-x) g(x)\, dx. \tag{A17}$$

If one considers $g = J_x$ or J_z as in (17), and f equal to the ξ_{em} (or η_{em}) or ξ_{om} (or η_{om}) parts (indicate parts by $\xi'_{(e,o)m}$ or $\eta'_{(e,o)m}$) of E_z or E_x in (A6) or (A8), noting that $f(-x) = \pm f(x)$ depending on symmetry, the assumption of perfect conductors leading to complementary current and field parts makes the right-hand side of (A17) zero.

Now examine (17) relating coupled slot fields and surface currents by the anisotropic $\tilde{G}$ dyadic. Multiply (17a) by $\tilde{\eta}'_{ej}$, $\tilde{\eta}'_{oj}$ and (17b) by $\tilde{\xi}'_{ej}$, $\tilde{\xi}'_{oj}$; then the spectral sum (we can employ $n = 1, 2, \cdots$ due to symmetry if desired) is

$$\sum_{n=-\infty}^{\infty} \tilde{\eta}'_{ej} \tilde{G}'_{11}(\gamma, n) \tilde{E}_x(n) + \sum_{n=-\infty}^{\infty} \tilde{\eta}'_{ej} \tilde{G}'_{12}(\gamma, n) \times \tilde{E}_z(n) = 0, \qquad j = 1, 2, \cdots, n_x \tag{A18a}$$

$$\sum_{n=-\infty}^{\infty} \tilde{\eta}'_{oj} \tilde{G}'_{11}(\gamma, n) \tilde{E}_x(n) + \sum_{n=-\infty}^{\infty} \tilde{\eta}'_{oj} \tilde{G}'_{12}(\gamma, n) \times \tilde{E}_z(n) = 0, \qquad j = 1, 2, \cdots, n_x \tag{A18b}$$

$$\sum_{n=-\infty}^{\infty} \tilde{\xi}'_{ej} \tilde{G}'_{21}(\gamma, n) \tilde{E}_x(n) + \sum_{n=-\infty}^{\infty} \tilde{\xi}'_{ej} \tilde{G}'_{22}(\gamma, n) \times \tilde{E}_z(n) = 0, \qquad j = 1, 2, \cdots, n_z \tag{A18c}$$

$$\sum_{n=-\infty}^{\infty} \tilde{\xi}'_{oj} \tilde{G}'_{21}(\gamma, n) \tilde{E}_x(n) + \sum_{n=-\infty}^{\infty} \tilde{\xi}'_{oj} \tilde{G}'_{22}(\gamma, n) \times \tilde{E}_z(n) = 0, \qquad j = 1, 2, \cdots, n_z. \tag{A18d}$$

Treat the even-mode coupled slot situation by placing (A10) into (A18) grouping spectrally summed terms using $\tilde{\eta}'_{ej} = \sin(\alpha_n s)\tilde{\eta}_{ej}$, $\tilde{\eta}'_{oj} = \cos(\alpha_n s)\tilde{\eta}_{oj}$, $\tilde{\xi}'_{ej} = \cos(\alpha_n s)\tilde{\xi}_{ej}$, $\tilde{\xi}'_{oj} = \sin(\alpha_n s)\tilde{\xi}_{oj}$, and defining

$$X_{11}^{jm11} = \sum_{n=-\infty}^{\infty} \sin^2(\alpha_n s) \tilde{\eta}_{ej} \tilde{G}'_{11} \tilde{\eta}_{em} \tag{A19a}$$

$$X_{11}^{jm12} = \sum_{n=-\infty}^{\infty} \sin(\alpha_n s)\cos(\alpha_n s) \tilde{\eta}_{ej} \tilde{G}'_{11} \tilde{\eta}_{om} \tag{A19b}$$

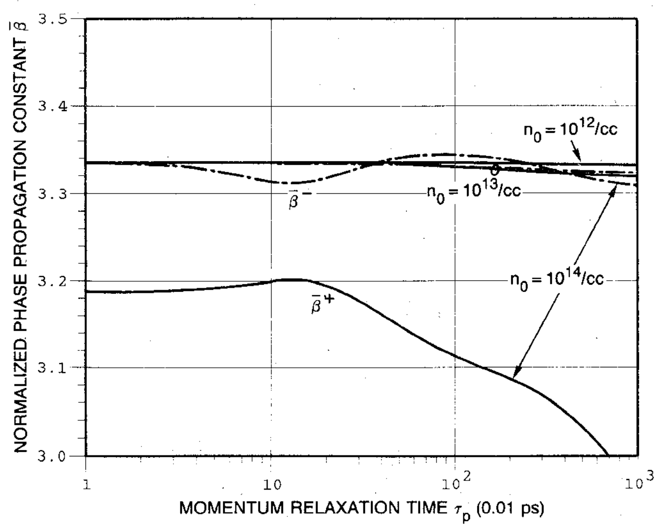

Fig. 14. Variation of $\bar{\beta}^+$ and $\bar{\beta}^-$ against τ_p for the Fig. 13(a) case. $n_0 = 10^{12}$, 10^{13}, and 10^{14}/cc.

$$X_{11}^{jm21} = \sum_{n=-\infty}^{\infty} \cos(\alpha_n s)\sin(\alpha_n s) \tilde{\eta}_{oj} \tilde{G}'_{11} \tilde{\eta}_{em} \tag{A19c}$$

$$X_{11}^{jm22} = \sum_{n=-\infty}^{\infty} \cos^2(\alpha_n s) \tilde{\eta}_{oj} \tilde{G}'_{11} \tilde{\eta}_{om} \tag{A19d}$$

$$X_{12}^{jm11} = \sum_{n=-\infty}^{\infty} \sin(\alpha_n s)\cos(\alpha_n s) \tilde{\eta}_{ej} \tilde{G}'_{12} \tilde{\xi}_{em} \tag{A19e}$$

$$X_{12}^{jm12} = \sum_{n=-\infty}^{\infty} \sin^2(\alpha_n s) \tilde{\eta}_{ej} \tilde{G}'_{12} \tilde{\xi}_{om} \tag{A19f}$$

$$X_{12}^{jm21} = \sum_{n=-\infty}^{\infty} \cos^2(\alpha_n s) \tilde{\eta}_{oj} \tilde{G}'_{12} \tilde{\xi}_{em} \tag{A19g}$$

$$X_{12}^{jm22} = \sum_{n=-\infty}^{\infty} \cos(\alpha_n s)\sin(\alpha_n s) \tilde{\eta}_{oj} \tilde{G}'_{12} \tilde{\xi}_{om} \tag{A19h}$$

$$X_{21}^{jm11} = \sum_{n=-\infty}^{\infty} \cos(\alpha_n s)\sin(\alpha_n s) \tilde{\xi}_{ej} \tilde{G}'_{21} \tilde{\eta}_{em} \tag{A19i}$$

$$X_{21}^{jm12} = \sum_{n=-\infty}^{\infty} \cos^2(\alpha_n s) \tilde{\xi}_{ej} \tilde{G}'_{21} \tilde{\eta}_{om} \tag{A19j}$$

$$X_{21}^{jm21} = \sum_{n=-\infty}^{\infty} \sin^2(\alpha_n s) \tilde{\xi}_{oj} \tilde{G}'_{21} \tilde{\eta}_{em} \tag{A19k}$$

$$X_{21}^{jm22} = \sum_{n=-\infty}^{\infty} \sin(\alpha_n s)\cos(\alpha_n s) \tilde{\xi}_{oj} \tilde{G}'_{21} \tilde{\eta}_{om} \tag{A19l}$$

$$X_{22}^{jm11} = \sum_{n=-\infty}^{\infty} \cos^2(\alpha_n s) \tilde{\xi}_{ej} \tilde{G}'_{22} \tilde{\xi}_{em} \tag{A19m}$$

$$X_{22}^{jm12} = \sum_{n=-\infty}^{\infty} \cos(\alpha_n s)\sin(\alpha_n s) \tilde{\xi}_{ej} \tilde{G}'_{22} \tilde{\xi}_{om} \tag{A19n}$$

$$X_{22}^{jm21} = \sum_{n=-\infty}^{\infty} \sin(\alpha_n s)\cos(\alpha_n s) \tilde{\xi}_{oj} \tilde{G}'_{22} \tilde{\xi}_{em} \tag{A19o}$$

$$X_{22}^{jm22} = \sum_{n=-\infty}^{\infty} \sin^2(\alpha_n s) \tilde{\xi}_{oj} \tilde{G}'_{22} \tilde{\xi}_{om} \tag{A19p}$$

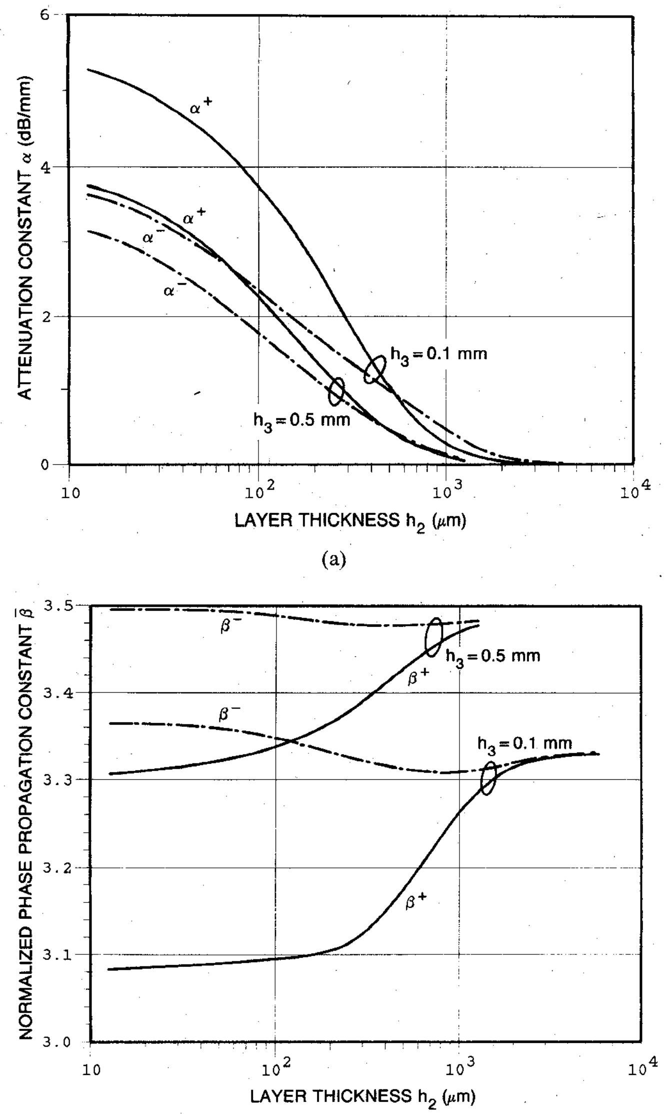

Fig. 15. (a) Variation of α^+ and α^- against h_2 for the Fig. 12(a) case. Here $B_0 = 10$ kG and $w = 0.2$ mm with $h_3 = 0.1$ or 0.5 mm. (b) Variation of $\bar{\beta}^+$ and $\bar{\beta}^-$ against h_2 for the Fig. 15(a) case.

one obtains

$$\sum_{m=1}^{n_x} S_{11}^{jm}\begin{bmatrix} a'_{m1} \\ b'_{m1} \end{bmatrix} + \sum_{m=1}^{n_z} S_{12}^{jm}\begin{bmatrix} c'_{m1} \\ d'_{m1} \end{bmatrix} = 0, \qquad j = 1, 2, \cdots, n_x \tag{A20a}$$

$$\sum_{m=1}^{n_x} S_{21}^{jm}\begin{bmatrix} a'_{m1} \\ b'_{m1} \end{bmatrix} + \sum_{m=1}^{n_z} S_{22}^{jm}\begin{bmatrix} c'_{m1} \\ d'_{m1} \end{bmatrix} = 0, \qquad j = 1, 2, \cdots, n_z \tag{A20b}$$

where S_{11}^{jm}, S_{12}^{jm}, S_{21}^{jm}, and S_{22}^{jm} are $n_x \times n_x$, $n_x \times n_z$, $n_z \times n_x$, and $n_z \times n_z$ sized matrices, and

$$S_{kl}^{jm} = \begin{bmatrix} X_{kl}^{jm11} & X_{kl}^{jm12} \\ X_{kl}^{jm21} & X_{kl}^{jm22} \end{bmatrix}. \tag{A21}$$

Consequently, the anisotropic determinantal equation can be expressed in compact form as

$$\begin{bmatrix} S_{11} & S_{12} \\ S_{21} & S_{22} \end{bmatrix} [v_1 v_2 \cdots v_{n_x} w_1 w_2 \cdots w_{n_z}]^T = 0 \tag{A22}$$

where

$$v_m = \begin{bmatrix} a'_{m1} \\ b'_{m1} \end{bmatrix} \qquad w_m = \begin{bmatrix} c'_{m1} \\ d'_{m1} \end{bmatrix} \tag{A23}$$

or, in the most abbreviated form, as

$$S\begin{bmatrix} v \\ w \end{bmatrix} = 0. \tag{A24}$$

It is the solution to $\det S(\gamma) = 0$ which we seek, $\gamma = \gamma+, \gamma-$. For the odd-mode coupled slot situation, use of (A13) leads to the (A24) form if all $\sin(\alpha_n s)$ and $\cos(\alpha_n s)$ factors are interchanged in (A19) and double primed notation is adopted in (A23).

References

[1] B. R. McLeod and W. G. May, "A 35 GHz isolator using a coaxial solid-state plasma in a longitudinal magnetic field," *IEEE Trans. Microwave Theory Tech.*, vol. MTT-19, pp. 510–516, June 1971.

[2] A. V. Nurmikko, D. M. Bolle, and S. Talisa, "Guiding and control of millimeter waves by surface plasmon phenomena in semiconductors," *Int. J. Infrared Millimeter Waves*, vol. 1, pp. 3–13, 1980.

[3] D. M. Bolle and S. H. Talisa, "Fundamental considerations in millimeter and near-millimeter component design employing magnetoplasmons," *IEEE Trans. Microwave Theory Tech.*, vol. MTT-29, pp. 916–923, Sept. 1981.

[4] S. H. Talisa and D. M. Bolle, "Performance predictions for isolators and differential phase shifters for the near-millimeter wave range," *IEEE Trans. Microwave Theory Tech.*, vol. MTT-29, pp. 1338–1343, Dec. 1981.

[5] W-L. Hwang, S. H. Talisa, and D. M. Bolle, "New results for near-millimeter wave isolators and phase shifters based on magnetoplasmons on GaAs substrates," *Int. J. Infrared Millimeter Waves*, vol. 3, pp. 253–263, 1982.

[6] E. M. Godshalk and F. J. Rosenbaum, "Nonreciprocal effects in semiconductor loaded waveguide at millimeter wavelengths," *IEEE MTT-S Int. Symp. Dig.*, June 1984, pp. 455–456.

[7] C. M. Krowne, "Fourier transformed matrix method of finding propagation characteristics of complex anisotropic layered media," *IEEE Trans. Microwave Theory Tech.*, vol. MTT-32, pp. 1617–1625, Dec. 1984.

[8] A. A. Mostafa, C. M. Krowne, and K. A. Zaki, "Numerical spectral matrix method for propagation in general layered media: Application to isotropic and anisotropic substrates," *IEEE Trans. Microwave Theory Tech.*, vol. MTT-35, pp. 1399–1407, Dec. 1987.

[9] E. D. Palik and J. K. Furdyna, "Infrared and microwave magnetoplasma effects in semiconductors," *Rep. Progr. Phys.*, vol. 33, pp. 1193–1322, 1970.

[10] C. M. Krowne, "Perturbational solutions of the Boltzmann transport equation for n^+nn^+ structures," *Proc. Inst. Elec. Eng.*, vol. 134, pt. I, pp. 93–100, June 1987.

[11] F. J. Blatt, *Physics of Electronic Conduction in Solids*. New York: McGraw-Hill, 1968.

[12] S. M. Sze, *Physics of Semiconductor Devices*. New York: Wiley, 1981.

Clifford M. Krowne (S'73–M'74–SM'84) attended the University of California, Berkeley, and received the B.S. degree in physics from the University of California, Davis, in 1970 and the M.S. and Ph.D. degrees in electrical engineering from the University of California, Los Angeles, in 1972 and 1975, respectively.

In 1970, he was employed in the Microelectronics Division of Lockheed Missiles and Space Company. In 1976 he joined the technical staff of the Watkins-Johnson Company in Palo Alto, CA, and in 1978 he became a faculty member in the Department of

Electrical Engineering at North Carolina State University, Raleigh. Dr. Krowne has been a consultant to several industrial firms and was a 1980 ASEE Summer Faculty Fellow at the NASA Johnson Space Center, Houston, TX. Since 1982, he has been with the Electronics Science and Technology Division of the Naval Research Laboratory, Washington, DC, studying microwave and millimeter-wave properties of active and passive solid-state devices. He is also an Adjunct Professor of Electrical Engineering at the University of Maryland, College Park.

Dr. Krowne has published over 80 technical papers in solid-state electronics, microwave circuits, electromagnetics, and engineering education. He has served on the technical program conference committees of the Antennas and Propagation Society and the Microwave Theory and Techniques Society and chaired sessions in the electromagnetic theory, microstrip antenna, and solid-state devices/circuits areas. Dr. Krowne was a member of the 1987 MTT Symposium Steering Committee. He is a member of Phi Kappa Phi, Tau Beta Pi, and the American Physical Society.

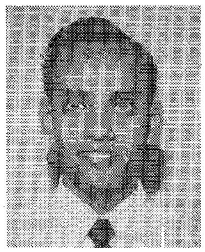

Ayman A. Mostafa (S'85) was born in Cairo, Egypt, in 1959. He received the B.Sc. (with honors) and M.Sc. degrees in electrical engineering from Ain Shams University, Cairo, in 1981 and 1984, respectively.

From 1981 to 1984 he was a Teaching Assistant in the Department of Electronics and Computer Engineering at Ain Shams University. From February 1985 to September 1985 he was a Research Associate at Duisburg University, West Germany. In September 1985 he joined the Electrical Engineering Department of the University of Maryland as a graduate Research Assistant and since then has been working towards the Ph.D. degree. His research interests include the CAD of millimeter-wave circuits and numerical solutions of planar microwave structures.

Kawthar A. Zaki (SM'85) received the B.S. degree (with honors) from Ain Shams University, Cairo, Egypt, in 1962 and the M.S. and Ph.D. degrees from the University of California, Berkeley, in 1966 and 1969, respectively, all in electrical engineering.

From 1962 to 1964, she was a Lecturer in the Department of Electrical Engineering, Ain Shams University. From 1965 to 1969, she held the position of Research Assistant in the Electronic Research Laboratory, University of California, Berkeley. She joined the Electrical Engineering Department, University of Maryland, College Park, in 1970, where she is presently Professor of Electrical Engineering. Her research interests are in the areas of electromagnetics, microwave circuits, optimization, computer-aided design, and optically controlled microwave and millimeter-wave devices.

Dr. Zaki is a member of Tau Beta Pi.